Basin Research

WILEY

Basin Research IAS EAGE

RESEARCH ARTICLE OPEN ACCESS

Deconvolving the Effects of Fluvial Transit and Storage on Preservation of Sedimentary Source Signals Using Heavy Minerals and Terrestrial Biomarkers

Sophia Dosch[1,2] | Niels Hovius[1,2] | Sergio Andò[3] | Eduardo Garzanti[3] | Marisa Repasch[4] | Joel Scheingross[5] | Dirk Sachse[1,6]

[1]GFZ German Research Centre for Geosciences, Potsdam, Germany | [2]Institute of Geosciences, Universität Potsdam, Potsdam, Germany | [3]Laboratory for Provenance Studies, University of Milano-Bicocca, Milano, Italy | [4]Department of Earth and Planetary Sciences, University of New Mexico, Albuquerque, New Mexico, USA | [5]Department of Geological Sciences and Engineering, University of Nevada Reno, Reno, Nevada, USA | [6]Department of Geography, Humboldt Universität zu Berlin, Berlin, Germany

Correspondence: Sophia Dosch (sophia.dosch@gfz-potsdam.de)

Received: 30 August 2024 | **Revised:** 15 November 2025 | **Accepted:** 22 November 2025

ABSTRACT

Analysis of naturally occurring markers of environmental signals, or proxy analysis, in sedimentary records can yield valuable insights into the geologic past. However, these proxies may be altered between sediment source and sink by selective gain, loss, or transformation of individual organic or inorganic components. To aid interpretation of sedimentary proxies, we must understand physical and chemical processes occurring during transit. We track the provenance and transformation of two commonly used proxies, long-chain *n*-alkanes and heavy minerals, between source and sink along the Río Bermejo, a lowland alluvial river without significant tributaries or distributaries, traversing the east Andean foreland basin. Our sampling strategy allowed determining the sediment input signal and isolating the effects of long-range transport and transient floodplain storage. Fine-grained sediments present in the suspended load and deposited in floodplains show heavy nC_{29} *n*-alkane δ^2H values compared to channel bed sediment. Heavy nC_{29} *n*-alkane δ^2H values indicate that organic matter in suspended and deposited sediments was sourced from low elevations, while light nC_{29} *n*-alkane δ^2H values indicate upland sources for the bed sediment. These data suggest that organic matter proxies in finer sediment are overprinted during transient floodplain storage, while organic matter travelling near the river bed is transferred downstream efficiently without significant recycling. Meanwhile, a negative correlation of Zircon-Tourmaline-Rutile index and corroded grains of all samples indicates progressive weathering of silicate minerals during transient foreland sediment storage. In particular, sediment deposited on the floodplain is depleted in clinopyroxenes and amphiboles compared to suspended sediment. Combining the physical and chemical characteristics of organic and inorganic proxies can help isolate source area fingerprints and identify the effects of lowland fluvial transit on sedimentary records. This improves our understanding of how source-to-sink processes influence the preservation of proxy signals, their transfer into the stratigraphic record, and the potential impacts of flood basin sediment storage on biogeochemical cycles.

1 | Introduction

Sediments in depositional basins carry the imprints of their source area, but they may also bear the signal of physical and chemical processes active during erosion, transport and deposition (Tofelde et al. 2021; Garzanti et al. 2020; Jerolmack and Paola 2010). While the lithology of the source is reflected in the mineralogy of the sediment, the organic fraction of the sediment can carry information about the elevation, climate and ecology of the source area (e.g., Mclennan et al. 1993, Walker

Highlights

- Sediment transport modes (e.g., bedload, suspension, intermittent deposition) have different effects on the preservation and alteration of source signals in organic and clastic proxies.
- Suspendable sediments undergo weathering and organic matter replacement during transient floodplain storage.
- Bed sediments are transferred rapidly, without intermittent storage on the floodplain.
- Combined analyses of heavy minerals and long-chain *n*-alkanes can be used to distinguish between source and transit effects on sedimentary proxies.

and Richardson 1991, Nicholls 1963). Grain-size distribution and grain shapes may be set initially by the geomorphic process causing sediment mobilisation (Sklar 2024).

After mobilisation, sediment is transported by rivers as bedload or in suspension and is prone to intermittent deposition on adjacent floodplains, and reworking into the active channel before delivery to a depositional basin. Along this potentially protracted trajectory, sediments can be subject to chemical and physical alterations, such as mechanical abrasion and weathering and, in the case of organic matter (OM), mineralization (e.g., Resentini et al. 2018; Andò et al. 2013; Koiter et al. 2013; Morton and Smale 1990). These alterations can obscure the source signal, complicating the interpretation of sediment generation and flux from downstream sediment characteristics (e.g., Dellinger et al. 2023; Regnier et al. 2022; Liu et al. 2022; Feng et al. 2016; Garzanti et al. 2011, 2010), and complicate the distinction between processes such as transport, intermittent storage and subsequent abrasion, as well as weathering and mineralization, and their order of occurrence (Andò et al. 2012; Stieglitz and Rothwell 1978). The degree to which characteristics of the sediment are altered, however, is not uniform. While some minerals are durable, others get weathered and break down more easily (Dryden and Dryden 1946). Similarly, some organic compounds are more resilient than others (e.g., Strosser 2010). Sedimentary provenance research focuses on durable sediment components to trace material origins, despite potential alterations during transport and storage.

In addition, there may be valuable information about transfer processes and conditions that can be gleaned with a careful use of proxies. A sedimentary proxy carries measurable characteristics of a specific sedimentary compound which may be used as a tracer of the sediment production and movement (e.g., Mann et al. 1999; Elias 2013). An effective method to deconvolve source and transit effects on proxies requires a combination of indicators that may be influenced in complementary ways by ambient conditions along the sediment pathway. Exploring the potential of this approach requires working in an active sediment routing system, specifically in a river system of sufficient size to allow observation of the alteration of known sediment source signals by long-range transport and transient deposition. We employ two commonly used sedimentary proxies, organic long-chain *n*-alkanes and inorganic heavy minerals along the Río Bermejo, NW Argentina. The Río Bermejo traverses the east Andean foreland basin as a free-flowing river between the mountain front and its confluence with the Río Paraguay along a 1300 km flow path without significant tributary input (Figure 1). The headwater sediment supply to the lowlands can be characterised at the mountain front. Downstream of this point, the suspended load of the river is cyclically deposited in and eroded from floodplains before entering the Río Paraguay (Repasch et al. 2020). This makes the Río Bermejo an ideal setting to assess the impact of modern pre and post-depositional alterations on the sediment suite, and to understand how these modifications and fluvial transport modes control the provenance signal carried by the river sediment (Garzanti et al. 2020).

Long-chain *n*-alkanes in organic matter and heavy minerals in the clastic sediment have different origins and refractivities. The heavy mineral suite is used to trace the provenance of sediment and can provide relevant information on tectonic processes (Morton 1985; Haughton et al. 1991; Garzanti et al. 2011, 2010, 2005). Surface texture of heavy minerals, ranging from unweathered to skeletal and from euhedral to rounded or broken, provides information on chemical weathering and mechanical abrasion (Andò et al. 2012; Moral Cardona et al. 2005; Morton and Smale 1990; Stieglitz and Rothwell 1978). Long-chain *n*-alkanes are abundant in terrestrial plant tissue. They are resistant to alteration, prone to preservation in sediment, can record information about the source elevation and source plant type in their isotopic composition, and may reflect the mobilisation and recycling of organic soil materials across a catchment (e.g., Cranwell 1972).

Galy et al. (2008) combined organic and clastic sediment characteristics of suspended sediment and bedload of the Ganga and Brahmaputra. They conclude that variations in the combined organic and clastic characteristics are related to hydrodynamic forces in the river, and the oxidation and replacement of organic matter during floodplain transit. To our knowledge, Andò et al. (2019) is the only previous study that combined *n*-alkanes and heavy minerals. They investigated the provenance of Indus Fan sediments and documented marine and terrestrial origin of OM associated with siliciclastic Himalayan detritus. We extend this approach to a modern fluvial system, where the systematic comparison of organic and inorganic proxies provides insight into sediment provenance and alteration during transit. First, we aim to reconstruct the provenance signal of the inorganic and organic fractions of the Río Bermejo sediment using heavy minerals and long-chain *n*-alkanes as proxies for these inorganic and organic characteristics, respectively. Second, we aim to isolate and understand the imprint of sediment cycling during transit. Finally, we consider how the combination of these complementary proxies may help to refine sediment provenance diagnoses. To address our aims, we have analysed a set of suspended load, bedload, and overbank sediment samples collected along the length of the Río Bermejo.

2 | Background and Conceptual Framework

To gain a mechanistic understanding of sediment movement between source and sink, we need a general framework on the sediment trajectories in the Río Bermejo's routing system.

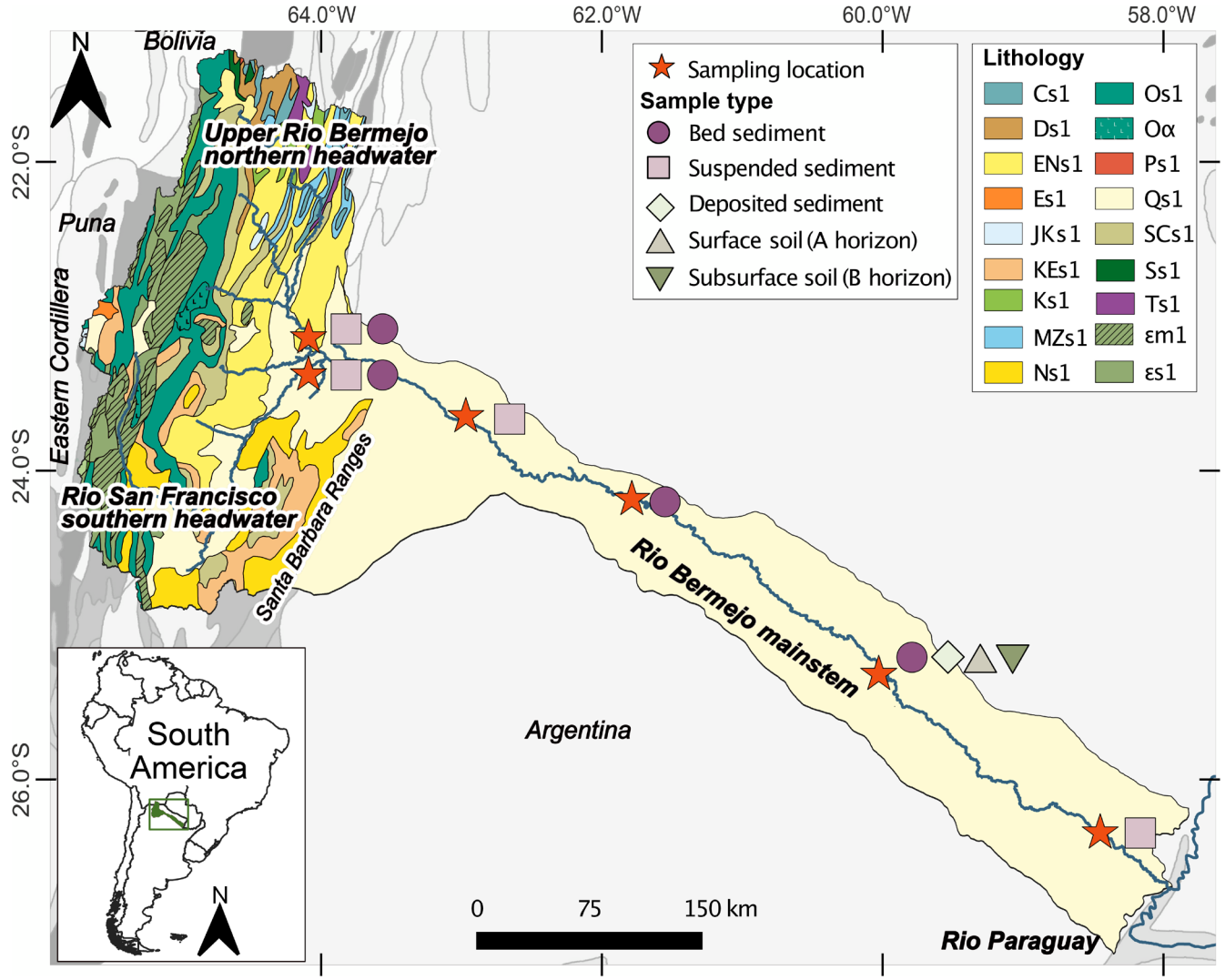

FIGURE 1 | Study area with a generalised geologic map (Gomez Tapias et al. 2019), including sampling sites and sample types collected at each site. Lithological, abbreviation: Cs1, Carboniferous Sedimentary Siliclastic; Ds1, Devonian Sedimentary Siliclastic; ENs1, Paleogene to Neogene Sedimentary Siliclastic; Es1, Paleogene Sedimentary Siliclastic; JKs1, Jurassic to Cretaceous Sedimentary Siliclastic; KEs1, Cretaceous to Paleogene Sedimentary Siliclastic; Ks1, Cretaceous Sedimentary Siliclastic; MZs1, Mesozoic Sedimentary Siliclastic; Ns1, Neogene Sedimentary Siliclastic; Os1, Ordovician Sedimentary Siliclastic; Oα, Ordovician Volcanic Rhyolitic; Ps1, Permian Sedimentary Siliclastic; Qs1, Quaternary Sedimentary Siliclastic; SCs1, Silurian to Carboniferous Sedimentary Siliclastic; Ss1, Silurian Sedimentary Siliclastic; Ts1, Triassic Sedimentary Siliclastic; εm1, Cambrian low to medium Metamorphic; εs1, Cambrian Sedimentary Siliclastic.

Our framework is conceived as follows: large amounts of sediment are mobilised in the Andean headwaters and transferred quickly downstream into the Río Bermejo mainstem. In the low-gradient foreland section of the Río Bermejo, suspended sediment is transported downstream over millennia through repetitive deposition on the floodplain and re-entrainment into the channel (Repasch et al. 2021). The suspended fraction is prevalent in the upper part of the river water column and prone to overbank spilling, unlike bedload. If overbank flooding syphons off water from the top of the water column, then hydrodynamic sorting may affect which sediment attributes get translated laterally into floodplain deposits (Garzanti et al. 2020). Deposited sediment is likely subjected to physical and chemical alterations such as mineralization of OM and weathering of clastic sediment to a greater extent than mobile sediment (Scheingross et al. 2019). Therefore, sediment sampled upstream of temporary storage may carry the unaltered source signal. In turn, the fluvial load sampled downstream of depositional storage may carry the source signal and the imprints of transit alterations alike. Mixing of progressively degraded and pre-weathered sediment with freshly supplied sediment may dampen both source and transit signals. Suspension sorting tends to concentrate coarser and denser grains near the channel bed, hampering the dynamic exchange of these grains with the floodplain. Above the threshold for grain motion, bedload therefore progresses downstream efficiently, likely on shorter timescales, without significant transient storage (Dosch, Hovius, Repasch, et al. 2024; Heijnen et al. 2022).

Bedload may possibly be stored temporarily on point bars, though the timescales and frequency of such storage deserve additional research. Point bars are largely composed of finer sediments and are reworked over shorter timescales than the entire floodplain. Consequently, these different transport modes may

be reflected in the different characteristics of suspended sediment undergoing intermittent storage regularly versus bedload sediment. Moreover, they may affect the *n*-alkane and heavy mineral fractions of fluvial sediment differently.

Stable carbon ($\delta^{13}C$) and hydrogen ($\delta^{2}H$) isotopic values in *n*-alkanes inform about ecosystem and environmental conditions at the OM source (e.g., Märki et al. 2020; Hoffmann et al. 2016; Ponton et al. 2014). The fractionation of $\delta^{2}H$ and $\delta^{13}C$ values in plant tissue is dependent on environmental conditions and plant type (e.g., Walker and Richardson 1991; Allison et al. 1984; Stewart and Taylor 1981). $\delta^{13}C$ values can distinguish C3 or C4 metabolic pathways of vegetation (Garcin et al. 2014; Tipple and Pagani 2013). Meanwhile, *n*-alkane $\delta^{2}H$ values are source tracers in mountain catchments with variable water $\delta^{2}H$ values due to effects of elevation and atmospheric water vapour trajectories (Hou et al. 2008; Sachse et al. 2012; Chikaraishi et al. 2004; Hassenruck-Gudipati et al. 2023). The depletion of heavy isotopes with increasing altitude (Dansgaard 1964), known as the altitude effect, is translated into plant OM (Ziegler et al. 1976). On a molecular level, the carbon preference index (CPI) indicates the odd-over-even chain length abundance, where a dominance of even chain lengths is characteristic for chemical maturity of *n*-alkanes (e.g., Bray and Evans 1961). This can be used as an indicator of processes during storage: CPIs > 10 indicate a predominance of fresh OM, whereas CPI < 1 is characteristic of fossil matter; intermediate values signal OM decay.

The content of heavy minerals (minerals with a density $> 2.90\,g\,cm^{-3}$) in river sediment is first determined at source by the mineralogy of headwater rocks. Source composition and texture are subsequently affected by hydraulic sorting during transport and deposition and/or weathering (Garzanti et al. 2020; Garzanti and Andò 2007; Morton and Smale 1990; Tejan-Kella et al. 1991). Ferromagnesian minerals tend to be more rapidly dissolved than other minerals even during shallow burial, thus markedly altering the heavy mineral suite in favour of durable species such as zircon, tourmaline and rutile (ZTR Index, Garzanti and Andò 2019, Morton and Hallsworth 2007, Hubert 1962). The degree of physical and chemical weathering of the heavy mineral suite may be derived from the grain surface texture (Andò et al. 2012; Tejan-Kella et al. 1991). Corrosion and weathering refer to the breakdown and alteration of mineral grains due to chemical processes, offering insights into the environmental conditions and duration of the depositional period. Rounding of grains is indicative of the mode and duration of transport (Garzanti 2017).

From this general framework we hypothesize that the imprints of chemical reactions on the sediment are predominantly imposed on the river sediment during temporary deposition. We expect the *n*-alkanes source signal in the floodplain deposited sediment to be recycled during foreland transit, leading to progressive overprinting with a foreland signal of $\delta^{2}H$ and $\delta^{13}C$ values, as well as with OM with higher CPI values with distance downstream, as also observed in the Brahmaputra basin (Galy et al. 2011). Conversely, if the fluvial load remains unaltered by intermittent deposition, it may carry the source signal. Notably, bedload transport without intermittent storage may not allow for recycling of recalcitrant OM or significant weathering of the mineral fraction, possibly permitting the unaltered transmission of the source signal regardless of sampling location. If signals can be deconvolved, insights into sediment sourcing, transport and transient storage can be used to determine characteristics of local biogeochemical cycles in headwaters and along the fluvial network. Location and timescales of OM recycling and mineral weathering determine the carbon budget of a landscape. If during intermittent storage, aged OM is respired, and siliciclastic detritus of the Río Bermejo is weathered, this may sensibly affect the carbon sequestration efficiency of a landscape over millennia.

3 | Materials and Methods

3.1 | Study Area: The Río Bermejo

The Río Bermejo is an undammed, quasi-natural sand bed river in northern Argentina with a catchment area of $120{,}300\,km^2$ (Sambrook Smith et al. 2016). Its two main headwater tributaries, the upper Río Bermejo and the Río San Francisco, comprising roughly half of the catchment area, drain the Andes and flow eastwards (Figure 1). These headwater streams converge in the Andean foothills at the town of Embarcacion, ~330 m asl, to form the Río Bermejo mainstem. The Río Bermejo mainstem traverses the flexural eastern Andean retroarc basin (Repasch et al. 2023; McGlue et al. 2016) without significant tributaries or distributaries and without substantial anthropogenic damming or drainage. This allows the river to remain free-flowing across the lowlands. The channel runs almost 1300 km before joining with the Río Paraguay.

The Andean retroarc foreland basin is chiefly filled with Pleistocene to Quaternary alluvium sourced from the adjacent Andes (Horton and Decelles 1997; Decelles 2012). The sediment source area comprises predominantly siliciclastic rocks ranging in age from Precambrian to Neogene (Gomez Tapias et al. 2019; McGlue et al. 2016; Sambrook Smith et al. 2016; Horton and Decelles 1997, Figure 1). The upper Río Bermejo and Río San Francisco carry lithoquartzose sand with siltstone/shale and metasiltstone/slate and rare volcanic and carbonate lithics. Detrital U–Pb zircon ages in retroarc basin sediments reflect significant recycling of Ordovician sedimentary and Precambrian metasedimentary rocks exposed in the Eastern Cordillera, Devonian sedimentary rocks exposed in the Inter-Andean fold-and-thrust belt, and Carboniferous to Cretaceous sedimentary rocks exposed in the Sub-Andean belt. Cretaceous zircon ages may also be sourced from small igneous outcrops in southern Bolivia. The youngest zircon U–Pb ages (~23–9 Ma) found in sediments in the distal retroarc basin represent more recent Andean volcanism (McGlue et al. 2016). Due to the lack of tributaries, a relatively uniform sediment mineralogical composition persists from the hinterland to the downstream reaches of the river (Repasch et al. 2020). Previous work has shown that sediments along the lowland Río Bermejo are depleted in feldspar, while the fraction of illite routinely exceeds 50% in sediment samples across the floodplain, which is indicative of silicate weathering in the basin (McGlue et al. 2016). Downstream fining and hydrodynamic sorting in the water column drives changes in the grain size distribution of river sediments with

increasing distance downstream (Repasch et al. 2020, 2022). Suspended and deposited sediments at the mountain front and bedload in the lowland reaches are very fine to medium sand (D_{50} = 107–280 μm), downstream deposited and suspended sediment range from silt to very fine sand (D_{50} = 8–90 μm) (Repasch et al. 2022).

Annually, ~103 Mt. of sediment are delivered from the mountains to the lowland river reach (Repasch et al. 2020), mainly during the wet season from January to April (Sambrook Smith et al. 2016). Lithospheric flexure controls flexural-bulge uplift in foreland, and is expressed in channel incision and accompanied by very high channel migration rates, averaging 14 m year^{-1} at 200–500 km linear distance downstream of the mountain front (Repasch et al. 2020, 2023). Repeated floodplain deposition, channel belt migration, and fluvial reworking in this rapidly migrating reach gives rise to the extended sediment transit times (Repasch et al. 2020; Sambrook Smith et al. 2016). Analysis of meteoric ^{10}Be shows that suspended load traversing the Río Bermejo foreland undergoes on average 4.5 erosion-deposition cycles, resulting in cumulative sediment transit times of 8520 ± 596 years near the confluence with the Río Paraguay (Greenberg et al. 2024; Repasch et al. 2020). Sediment storage times in abandoned channel belts can exceed 10,000 years (Scheingross et al. 2021). In contrast, at a flow rate of 1 m s^{-1} water traversing the foreland takes ~15 days to travel from the mountain front to the confluence with the Río Paraguay.

Precipitation in the Río Bermejo basin originates predominantly from the South Atlantic Ocean, recycled through the Amazon Basin and transported south-east by the South American low-level jet (Vera et al. 2006). The Chaco Low, a thermally and orographically induced low-pressure system, intensifies during the austral summer and draws in Atlantic-sourced air masses, enhancing moisture convergence and convection over the region (Salio et al. 2002). At higher altitudes, the Bolivian High and the Northwestern Argentinean Low form a vertical circulation pattern that reinforces convection and precipitation along the eastern flanks of the Andes (Seluchi et al. 2003; Vera et al. 2006). The northern headwater tributaries, draining steep, high-elevation terrain, are strongly influenced by this atmospheric regime, augmented by orographic forcing. In contrast, the southern headwaters of the Río Bermejo receive Atlantic-derived, monsoon-dominated moisture, but are less affected by the low-level Jet and Amazonian recycling due to the lower elevation and more southerly position. Across the foreland, precipitation declines from east to west as air masses lose moisture through rainout, creating a climatic gradient from the Dry Chaco to the Wet Chaco, where the lowermost part of the lowland basin has higher precipitation rates, resulting in wetland formation.

3.2 | Sampling and Sample Processing

3.2.1 | Sampling

Our sampling strategy exploits the unique absence of tributaries in the lowland Río Bermejo to isolate the effects of long-range fluvial transport and transient storage on the clastic and organic composition of sediments transported across the Andean foreland basin. During field campaigns in 2017, 2019 and 2020, we collected bed and suspended sediment from the active channel, overbank floodplain deposits of the active channel belt, and paleochannel deposits along the Río Bermejo mainstem (Table 1, Figure 1). We selected 14 samples to cover the range of sediment transport lengths and storage times in the system. They include four bedload and four suspended sediment samples collected from the active channel in April 2017, using a van Dorn style sampling bottle (Repasch et al. 2020). Aliquots of these samples were also used by Scheingross et al. (2021) and Repasch et al. (2022). Paired bed and suspended sediment samples were collected from each headwater tributary at the mountain front, at the southern headwater (Pichanal on the Río San Francisco (RSF), at 2 and > 3.5 m water depth, respectively), and the northern headwater (Embarcación on the upper Río Bermejo, at 1 and > 1.5 m water depth, respectively). The suspended and bedload samples from the upper Río Bermejo and the Río San Francisco are assumed to represent the headwater input into the mainstem. A third pair of suspended and bedload samples was collected from the lowland Río Bermejo, 422 km river length downstream, at Reserva Natural Formosa (RNF), at 2.5 and > 3.5 m depth. Finally, the downstream sediment composition is represented by a bedload sample at a river length of 865 km downstream at Puerto Lavalle (> 3.5 m depth), and a suspended sediment sample from 1221 km downstream, at General Mansilla (2.7 m depth).

In addition, six samples collected across a chronosequence of overbank and paleochannel deposits were utilised. We collected 5–20 g of sample material with a clean, stainless-steel trowel, then transferred into paper bags and air dried in the field before being oven-dried for up to 5 days at 35°C in the laboratory. One sample is a recent overbank deposit, adjacent to the active channel (sample AR20SD015-SD0). Two samples were collected in the active channel belt on the surface and from 40 cm depth, labelled as A and B horizon (sample AR20-SD015-S-0 and sample AR20SD015-S-40), with a minimum age of 21 years, as suggested by historical image analysis (Scheingross et al. 2021). Samples of older sediment include one from A horizon soil in a paleochannel with grassland and forest cover, ca. 14 km from the active channel (AR20SD016-S-0), with a minimum age of 150 years (Scheingross et al. 2021). Two more samples were collected from a paleochannel, ca. 15 km away from the active channel in 30 cm depth, labelled as A and B horizon (AR20SD017-S-0 and AR20SD017-S-30), with deposit ages of 60 and 1360 years, as determined using the radiocarbon content of charcoal and optically stimulated luminescence, respectively (Scheingross et al. 2021; Repasch et al. 2020).

3.2.2 | Heavy Minerals Analysis

Heavy minerals (density > 2.90 g cm^{-3}) were separated from the grain-size fraction 5–500 μm obtained by wet sieving of an aliquot of the disaggregated and homogenised bulk sediment. To elutriate the fraction < 5 μm, we mixed 1 g of sodium hexametaphosphate ($Na(PO_3)_6$) with 1 L tap water to deflocculate organo-mineral aggregates. The sediment-fluid mixture was stirred, and after 20 min settling time, the upper layer was skimmed to remove the fraction < 5 μm, repeatedly

TABLE 1 | Sample overview: Sample ID, Location name, coordinates, sample type, distance from mountain front, and age range. Min deposition age was estimated via optically stimulated luminesce and historical image analysis.

Sample ID	Location name	Latitude	Longitude	Sediment type	Fluvial transport distance to mountain front (km)[a]	Sample depth (m)[b]	Min. deposit age range (years)[c]	Bulk ^{14}C age (years)[d]
AR17MR-26	Embarcación	−23,2480	−64,1376	Suspended sediment	−10	2	n.a.	1965 ± 81
AR17MR-31	Pichanal	−23,3559	−64,1828	Suspended sediment	−15	0	n.a.	723 ± 72
AR17MR-14	RNF	−24,3133	−61,8379	Suspended sediment	422	2.5	n.a.	636 ± 75
AR17MR-05	General Mansilla	−26,6738	−58,6186	Suspended sediment	1221	2.7	n.a.	1020 ± 75
AR17MR-27	Embarcación	−23,2480	−64,1376	Near-bed sediment	−10	> 3	n.a.	5777 ± 113
AR17MR-30	Pichanal	−23,3559	−64,1828	Near-bed sediment	−15	> 1.5	n.a.	671 ± 88
AR17MR-17	RNF	−23,7513	−63,0526	Near-bed sediment	135	> 5	n.a.	n.a.
AR17MR-57	PLV	−25,6551	−60,1296	Near-bed sediment	865	> 3.5	n.a.	n.a.
AR20-SD015 Sed0	Active channel PLV	−25,6551	−60,1296	Deposited sediment	865	0	21-n.a.	n.a.
AR20-SD015 Soil0	Active channel PLV	−25,6551	−60,1296	Soil (A horizon)	865	0	21-n.a.	n.a.
AR20-SD015 Soil40	Active channel PLV	−25,6551	−60,1296	Soil (B horizon)	865	0.4	21-n.a.	n.a.
AR20-SD017 Soil0	Paleochannel PLV	−25,7925	−60,1468	Soil (A horizon)	865	0	60–1360	n.a.
AR20-SD017 Soil30	Paleochannel PLV	−25,7925	−60,1468	Soil (B horizon)	865	0.3	60–1360	n.a.
AR20-SD016 Soil0	Paleochannel Bermejito	−25,6111	−60,1468	Soil (A horizon)	865	0	150-n.a.	n.a.

Abbreviation: n.a., data not available.
[a]AR20-SD017 and AR20-SD016 are located 14 km linear distance, SW from the active channel. AR20-SD016 is located 29 km NE of AR20-SD017.
[b]Depth below the water surface for suspended and near-bed sediment samples; depth from the sediment surface for deposited sediment and soil samples.
[c]Published by Scheingross et al. (2021).
[d]Published by Repasch et al. (2021).

if necessary. The settled eluant was sieved through a 5 μm mesh. The samples AR20SD015-S-0, AR20SD016-S-0, and AR20SD017-S-0 were additionally treated with 100 mL 35% H_2O_2 to remove OM content before final sieving. All separated fractions were dried and weighed. To isolate the low-density and dense fractions, all samples were admixed with 100 mL sodium polytungstate (SOMETU-Europe, CAS #12333–13-0, density: 2.90 g cm^{-3}) and centrifugated before separating them over a paper filter. After washing with deionised water, the isolated dense fraction of each sample was mounted on a glass slide. Of each sample, at least 200 transparent heavy-mineral grains were point-counted under a polarising microscope, and the proportions among different mineral species were quantified. Mineral identifications were checked with Raman spectroscopy and surface features were systematically characterised following Andò et al. (2012). The heavy mineral and transparent heavy mineral concentrations (HMC, tHMC) are calculated as weight percentage of the bulk sample, and the Zircon-Tourmaline-Rutile index (ZTR) as the sum percentage of these three durable minerals in the point count (Hubert 1962). The Hornblende Colour Index (HCI) is based on the relative abundance of blue-green, green, green-brown and brown hornblende grains and can be used to trace metamorphic sediment provenance (Andò et al. 2013). Using a

polarising microscope, we distinguished five successive stages of chemical weathering: unweathered, corroded, etched, deeply etched, and skeletal (Andò et al. 2012). Unweathered grains show smooth surfaces with intact edges. Corroded grains display irregular outlines and surface pitting. Etched grains exhibit fine, linear or network-like surface patterns while retaining their overall shape. Deeply etched grains show intense surface etching with thinning and partial edge loss. Skeletal grains contain holes, furrows, grooves, and missing sections. The percentage of weathered heavy mineral grains is defined as the sum of corroded, (deeply) etched or skeletal grains in the point count. Further, we considered three stages of rounding: angular, subrounded or rounded. Angular grains feature sharp edges and flat surfaces. Subrounded grains show partially smoothed edges and slightly curved outlines. Rounded grains are characterised by smooth, curved surfaces and the absence of sharp edges. The percentage of rounded heavy minerals is defined as the sum of rounded and subrounded grains.

3.2.3 | Grain Size Analysis

The grain size distribution of six paleochannel and overbank sediment samples was measured using a Laser Diffraction Particle Size Analyser (Horiba LA950). For each sample, an aliquot of ~0.5–3 g of sediment was dispersed with 3 mL tetrasodium diphosphate ($Na_4P_2O_7$) and shaken for 12 h. The treated aliquot was measured tenfold, and the results averaged. All samples were measured with and without ultrasound to promote disaggregation but no significant difference between grain-size distributions was found. Values reported are from the runs without ultrasound. Grain-size distributions of suspended and bedload sediment samples, obtained with the same method, were previously published by Scheingross et al. (2021).

3.2.4 | *n*-Alkanes and Stable Isotopes Analysis

For extraction and measurement of long-chain *n*-alkanes, we followed Rach et al. (2020). We extracted *n*-alkanes from freeze-dried, grounded samples with 9:1 dichloromethane: methanol using a ThermoFisher Dionex Accelerated Solvent Extraction system and automated solid-phase extraction (SPE) using hexane as solvent. We evaluated OM maturity using the carbon preference index (CPI), determined after Bray and Evans (1961) for *n*-alkanes with 25–33 carbon atoms, using the sum of the concentration of odd-chained *n*-alkanes with chain lengths between 25 and 33, $\Sigma C_{25\text{-}33odd}$, and the sum of the concentration of even-chained *n*-alkanes with chain lengths between 24 and 34, $\Sigma C_{24\text{-}32even}$:

$$CPI_{25-33} = \frac{1}{2} \times \left(\frac{\Sigma C_{25-33odd}}{\Sigma C_{24-32even}} + \frac{\Sigma C_{25-33odd}}{\Sigma C_{26-34even}} \right) \quad (1)$$

We measured compound-specific hydrogen and carbon isotope ratios from the nC_{29} *n*-alkane (nC_{29} δ^2H and nC_{29} $\delta^{13}C$) in duplicates with a Trace GC 1310 (ThermoFisher Scientific) connected to a Delta V plus Isotope Ratio Mass Spectrometer (IRMS) (ThermoFisher Scientific). Hydrogen and carbon isotope ratios are expressed as ‰ deviations from Vienna Standard Mean Ocean Water, and the VPDB Vienna Pee Dee Belemnite standard, respectively. *n*-alkane data for the suspended and bedload samples (except nC_{29} δ^2H values of ARMR17-27 and ARMR17-46) were previously published by Repasch et al. (2022), and *n*-alkane data for the deposited samples were published by Dosch, Hovius, Ando, et al. (2024).

Previous studies found a statistically significant, linear relationship of nC_{29} δ^2H values with sampling elevation, ranging from about −110‰ in the lowland floodplain to about −180‰ in higher Andean headwaters, with elevation = $-6.4 \times nC_{29}$ δ^2H—640 (Dosch, Hovius, Repasch, et al. 2024; Nieto-Moreno et al. 2016; Rohrmann et al. 2014). We applied this linear relationship to separate between heavy, lowland-sourced and light, headwater-sourced *n*-alkanes, where the sample δ^2H value may reflect the averaged source elevation of the organic compound. For instance, δ^2H values around −145‰ would represent the elevation of the headwater tributary confluence of the upper Río Bermejo and Río Sao Francisco at 300 m asl. Using this threshold value enabled us to infer the dominant sourcing tendencies of sedimentary OM within the catchment. This assumes that orographic fractionation associated with the altitude effect is the primary control on the δ^2H variability (Nieto-Moreno et al. 2016, Rohrmann et al. 2014). For two samples with nC_{29} *n*-alkane concentrations too low for δ^2H measurement, we approximated the source elevation using nC_{31} δ^2H values. This approach was justified by a strong linear relationship between the nC_{29} δ^2H and nC_{31} δ^2H values in the study area (Dosch, Hovius, Repasch, et al. 2024).

3.2.5 | Estimates of Sediment Weathering During Deposition

To quantify the percentage change of amphibole and clinopyroxene during transit through the river system, we calculated their abundances relative to zircon, and normalised with respect to the ratio of these minerals in the bedload of the river. In doing so, we took advantage of zircon as a durable reference mineral, assuming that the bedload samples faithfully reflected the heavy-mineral composition at the source. We estimated the relative change ($Change_{X[i]}$, in %) in each sample type (i.e., deposited, suspended and bed sediment) as:

$$Change_X = \left[\frac{\frac{sample_X}{sample_{zircon}}}{\sum_1^n \left(\frac{source_X}{source_{zircon}} \right) \times n^{-1}} - 1 \right] \times 100 \quad (2)$$

Subscript *X* indicated the heavy mineral used, $Sample_X$ represented the fraction of the sample that is made up of mineral *X*. $Source_X$ was approximated using averaged bedload mineralogy, based on the assumption of conservative transport (see Section 2).

We estimated the mean time sediment spent in the river system before arriving at the sampling location (i.e., sediment transit time), using the fluvial transport distance of each sample (km, Table 1) and a virtual velocity of suspended sediment of 0.145 km $year^{-1}$ (Repasch et al. 2020). This allowed us to investigate

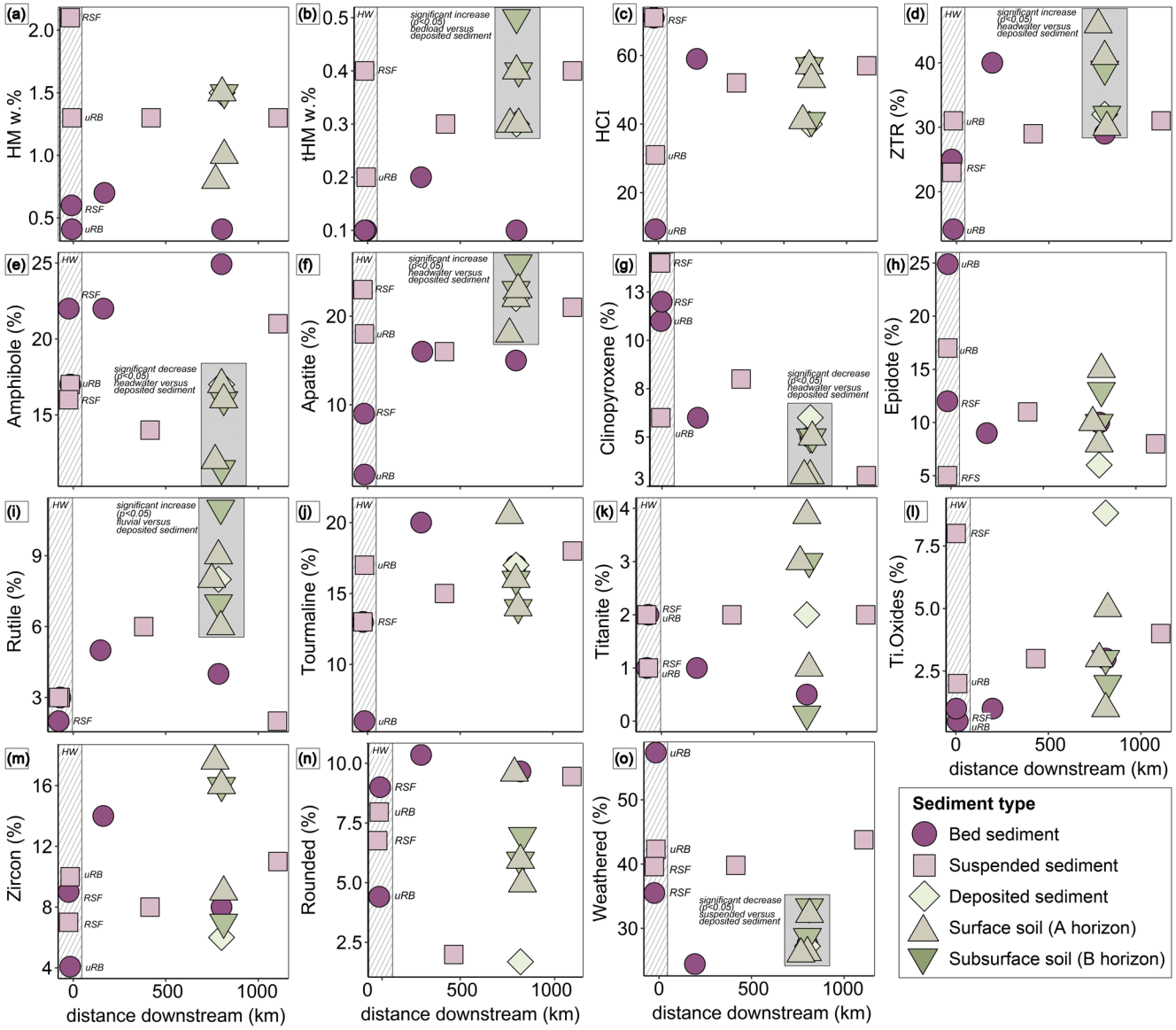

FIGURE 2 | Overview of (a) total heavy mineral concentration (HM, w.%), (b) transparent heavy mineral concentration (tHM, w.%), (c) Hornblende Colour Index (HCI), (d) Zircon-Tourmaline-Rutile (ZTR) index, as well as the percentage (grain count per 200 grains per sample) of common heavy minerals: (e) amphibole, (f) apatite, (g) clinopyroxene, (h) epidote, (i) rutile, (j) titanite, (k) titanium oxides, (l) tourmaline, (m) zircon, and the percentage of (n) rounded and (o) weathered grains in each sediment sample versus downstream distance. The light banded background highlights the headwater (HW) samples; sample origin is indicated as RSF (from southern Río San Francisco) and uRB (from northern upper Río Bermejo). Deposited samples are marked with a tightly banded background when there is a significant difference ($p < 0.05$) compared to other sample types and locations.

whether there is temporal control on mineralogical changes to the sediment.

3.3 | Data Analysis

All data analysis was performed using R 4.1.2 GUI 1.77 High Sierra build (8007). We used the Kolmogorov–Smirnov test to account for non-normal distribution of our data and the Mann–Whitney *U* test to test for significant differences between independent sample groups. The results are reported as mean ± standard deviation and range, respectively, the significance levels at the 95% confidence interval ($p < 0.05$), unless otherwise indicated.

4 | Results

4.1 | Heavy Minerals

4.1.1 | Heavy-Mineral Suite

The heavy-mineral concentration in the studied samples was low (HMC: 1.12 ± 0.4 wt.%, tHMC: 0.25 ± 0.1 wt.%, Figure 2a), chiefly reflecting widespread exposure of sedimentary rocks in the source area. Bedload HMC averages 0.5 ± 0.1 wt.% and tHMC 0.1 ± 0.2 wt.% without notable differences observed downstream in both indices (Figure 2a,b). Bedload ZTR ranges from 14 to 40 (Figure 2c). The heavy-mineral suite also did not show a clear downstream trend, excepting an increase in titanium oxides at the expense of epidote

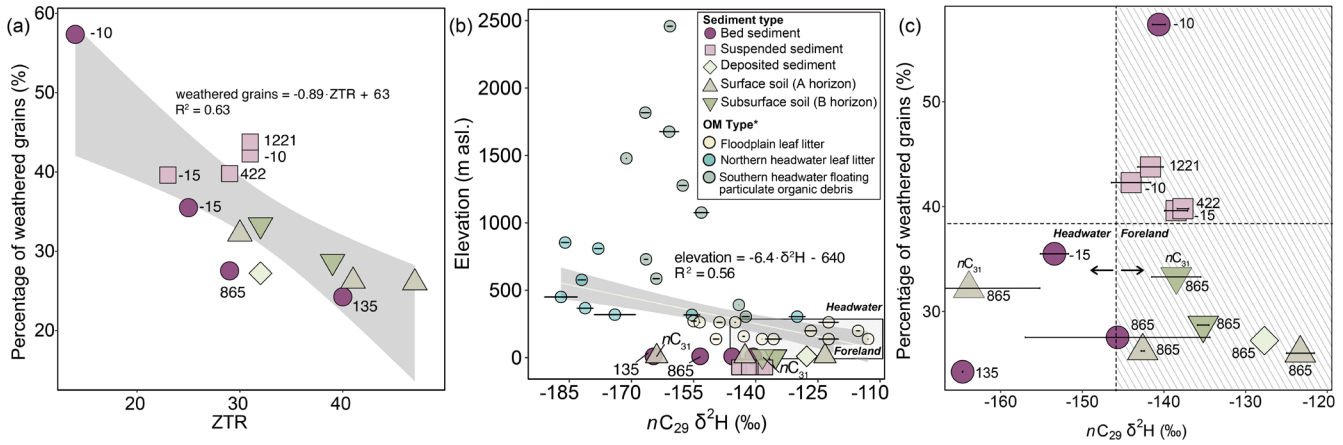

FIGURE 3 | (a) ZTR versus percentage of weathered heavy minerals (%). Linear regression ($p < 0.01$) was performed on all data points plotted. (b) Predicted sample source area, based on linear regression of elevation and nC_{29} δ^2H values of catchment floodplain and headwater leaf litter (Dosch, Hovius, Repasch, et al. 2024). Predicted source elevations of this study's data based on linear regression are shown on *y*-axis. Dotted lines illustrate regression for two example samples. Red numbers show nC_{31} δ^2H values of samples AR20-SD017 Soil0 and AR20-SD017 Soil30. (c) nC_{29} δ^2H and percentage of weathered grains. Background colours indicate foreland and headwater origin based on linear regression (panel a). Banded background marks indicate lower abundance of weathered grains. Error bars in panel (a and c) show standard deviation of duplicate measurements. Numbers next symbols indicate sampling location with distance downstream of suspended and bedload sediment.

(Figure 2e–l). Suspended-load HMC averaged 1.5 ± 0.4 wt.% and tHMC 0.3 ± 0.09 wt.%. As in bedload, notable differences downstream were not observed in HM and tHM, (Figure 2a,b). Suspended-load ZTR ranged from 23 to 31 (Figure 2c). The relative abundances of clinopyroxene and epidote tended to decrease downstream (clinopyroxene from 7% ± 3% to 3%, epidote from 12% ± 5% to 8%, Figure 2e–l). The deposited sediment HMC averaged 1.2 ± 0.3 wt.%, tHMC 0.3 ± 0.08 wt.%, and ZTR ranged from 30 to 37. Indices and relative heavy-mineral abundances showed no trend with depositional age (Figures S1 and S3).

Suspended and bedload samples from the upper Río Bermejo had a lower HCI (9–31 vs. 71–71), and less clinopyroxene (6%–11% 12–14 vs 12%–14%), but more epidote (17%–25% vs. 5%–12%) than samples from the Río San Francisco (Figure 2c,g,h). Other differences were minor.

A comparison among bedload, suspended load and deposited sediment indicated that tHMC was higher ($p < 0.05$) in the deposited sediment (0.3%–0.5%) than in bedload (0.1%–0.2%, Figure 2b). The deposited sediment had higher ZTR (30–47, $p < 0.05$) than suspended load and bedload (14–40, Figure 2d), less amphibole (11%–17%) than bedload (17%–25%) and suspended load (14%–21%, Figure 2e), and less ($p < 0.05$) clinopyroxene (3%–6%) than suspended load and bedload (6%–14%, Figure 2g). The downstream-most suspended sediment sample confirmed the downstream decreasing trend of clinopyroxene, whereas rutile and apatite increased ($p < 0.05$) from the upstream suspended load and bedload (rutile: 2%–3%; apatite: 2%–23%) to the deposited sediment (rutile: 6%–11%; apatite: 18%–26%, Figure 2f,i).

4.1.2 | Surface Textures

The percentage of rounded and weathered grains among all samples ranged from 1.4% to 10.4%, and from 24.2% to 57.3%, respectively. In bedload, rounded grains ranged from 4.4% to 10.4%, lacking the least rounded grains, and weathered grains ranged from 24.2% to 57.3%, with no clear downstream trend (Figure 2n,o). In the suspended load, rounded grains ranged from 1.9% to 9.4% also without a clear downstream trend, while the proportion of weathered grains was relatively constant, ranging from 39.6% to 42.7% (Figure 2n,o). In deposited sediment samples, rounded grains ranged from 1.4% to 9.5%, similar to the suspended load, and weathered grains from 26.0% to 33.3%, relatively uniform but somewhat less abundant than in the suspended load (Figure 2n,o). These metrics showed no discernible influence with depositional age. The Río San Francisco load had lower proportions of weathered grains (35.5%–39.6%) than the upper Río Bermejo load (42.2%–57.3%, Figure 2o).

ZTR and percentage of weathered grains were anti-correlated in our sample set (weathered = 0.89 × ZTR + 62.7, R^2 0.63, $p < 0.01$, see Figure 3a, where numbers next to the data points indicate downstream sampling distance). Bedload sediments distributed along this regression line. Suspended sediment samples had more weathered grains (39.6%–43.7%) and lower ZTR (23–31) than deposited sediment samples (26.0%–33.3% and 30–47, respectively).

4.2 | Grain Size

Throughout the catchment, bedload was coarser (133–322 μm) than the suspended load (9–150 μm, fining-upward in the water column; Repasch et al. 2022) and deposited sediments showed the finest grain sizes (3.4–67.5 μm, Figure S1). Apatite exhibited a negative linear relationship with median grain size ($y = -0.059x + 22$, $R^2 = 0.719$; $p < 0.05$), while other heavy minerals showed no such relationship (Figure S2).

4.3 | *n*-Alkanes

The carbon preference index (CPI) ranged from 0.31 to 11.6 in our sample set (Figure 4a). Bedload CPI was the lowest on average, with considerable variability (5.7 ± 5), contrasting with

a low variability of suspended sediment CPI (6.0 ± 0.5). Neither bedload nor suspended load samples displayed a discernable downstream trend in CPI. Slightly higher CPI values characterised the deposited sediments (6.6 ± 1), with no discernible trend related to depositional age. The *n*-alkane nC_{29} $\delta^{13}C$ values averaged −32.9‰ ± 5‰ (Figure 4b). Bedload values (−26.2‰ ± 11‰) were higher than suspended-load values (−35.4‰ ± 0.5‰), but neither showed a discernible downstream trend. Bedload sample AR17-MR30 yielded a significantly higher value (nC_{29} $\delta^{13}C = -18.4$‰). Deposited sediment nC_{29} $\delta^{13}C$ averaged −33.4‰ ± 2.3‰, somewhat higher than suspended-load values and without a discernible trend relating to depositional age. The nC_{29} $\delta^{2}H$ values ranged from −164.7‰ to −123.3‰ (Figure 4c). Bedload nC_{29} $\delta^{2}H$ values (−151.1‰ ± 10‰) were significantly lower ($p < 0.05$) than in suspended-load (−140‰ ± 3‰) and deposited sediments (−132.2‰ ± 8‰). For samples, AR20SD017-S-0 and AR20SD017-S-30, the nC_{29} alkane concentrations were too low to measure $\delta^{2}H$ values.

4.4 | Estimates of Sediment Weathering During Deposition

To estimate mineral loss due to weathering, we focused on two minerals, amphiboles and clinopyroxenes, because both exhibited a statistically significant loss in the deposited sediment. Using Equation (2), we estimated that 24%–76% (average 45%) of amphiboles and 22%–87% (average 61%) of clinopyroxenes were lost from river suspended load and deposit samples over a total transit time of around 8500 years (Figure 5). Using a Pearson correlation *t*-test, we found that the decreasing in amphibole abundance was not statistically significant. In contrast, the

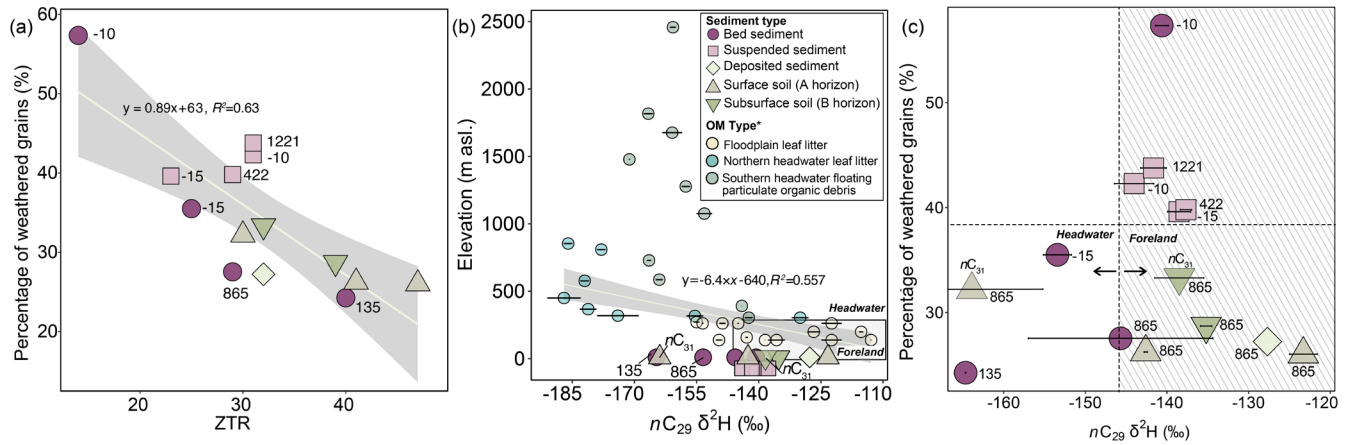

FIGURE 4 | Organic proxies with distance downstream, coloured by sediment type: (a) $CPI_{25\text{-}33}$, (b) nC_{29} $\delta^{13}C$ (‰), and (c) nC_{29} $\delta^{2}H$ (‰). Error bars represent standard deviations from duplicate measurements.

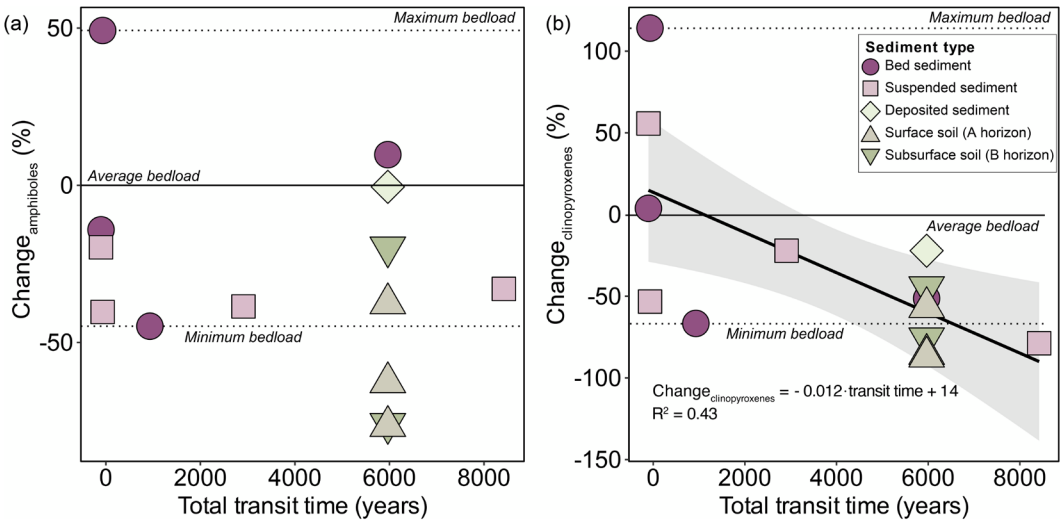

FIGURE 5 | Relative change (%) of ratio of (a) amphibole and (b) clinopyroxene to zircon of all samples compared to average amphibole and clinopyroxene to zircon ratio in bedload samples. Total transit time was estimated using a virtual velocity of 0.145 km year^{-1} (Repasch et al. 2020). Solid horizontal line represents average change of bed sediment ratios; horizontal dotted lines represent minimum and maximum change of bed sediment compared to bed average. Negative values indicate decreasing ratio compared to bed sediment.

decline in clinopyroxenes was statistically significant ($p < 0.01$), and followed a descending linear trend with transit time (Chang $e_{clinopyroxenes} = 14 - 0.012 \times$ total transit time, $R^2 = 0.43$).

5 | Proxy Alterations Reveal Source and Transit Effects in the Retroarc Foreland Basin

Using these results, we separately evaluate the variability in heavy minerals, texture, and *n*-alkane load during fluvial transit and transient floodplain storage. We then discuss how these findings combined reflect the sediment provenance signal and how they may help to inform our understanding of sediment cycling within the floodplain.

5.1 | Heavy Mineral Sourcing

The Río Bermejo heavy-mineral assemblage reflects provenance mostly from (meta) sedimentary rocks exhumed in the eastern Cordillera. In addition, clinopyroxene, hypersthene, oxy-hornblende, and green-brown magmatic hornblende signal contributions from andesitic-type volcanic rocks that are more abundant in the headwaters of Río San Francisco than farther north. Tributary inputs, including volcanic minerals, are mixed downstream of the confluence and the heavy-mineral suite is homogenised (cf. McGlue et al. 2016, Figure 1), indicating that the mixing process is controlled by tributary sediment load.

5.1.1 | Hydrodynamic Sorting

Hydrodynamic sorting during fluvial transport affects the distribution of grains with different size and density within the water column (Dietrich 1982; Rouse 1937) and should be taken into account when considering our results. In our sample set, hydrodynamic sorting in the water column is more strongly reflected in the finer particle size of the suspended load ($35.3 \pm 46\,\mu m$) than of the bedload ($202.0 \pm 85\,\mu m$), as well as in downstream fining previously described for the Río Bermejo (Repasch et al. 2022; McGlue et al. 2016). At a site, the measured suspended sediment grain-size reflects the depth in the water column from which a sample was collected (Repasch et al. 2022). The finest grains are transported at the top of the water column, and the fine nature of the sediment deposited in the foreland (Figure S1) indicates the important role of selective spilling of the finest fractions during overbank flooding (e.g., Allen 1964).

We rule out that downstream fining of the river load is caused significantly by grain comminution, because no downstream trend is observed in the relative abundance of rounded grains in any of the sampled sediment types (Figure 2n), and because the dominantly fine particle size dictates that impacts during fluvial transport are viscously damped (e.g., Scheingross et al. 2014; Joseph et al. 2001).

The effect of grain size on relative heavy-mineral abundances is evaluated using the median grain size D_{50} of each sample. The only heavy mineral showing a significant correlation with D_{50} is apatite, which is less abundant in bedload (Figure 2f) and more abundant in the finer sediment fraction (Figure S1). This implies that apatite is more concentrated in the upper part of the river water column, possibly due to its relatively low density ($\sim 3.2\,g\,cm^{-3}$) and/or predominantly small grain size. Sediment in the upper water column is most prone to overbank spilling. We speculate that the overbank deposition of apatite might be associated with minor flooding, transporting only the sediment of the upper water column onto the channel banks. In contrast, full-scale crevassing would divert the majority of the river sediment load away from the channel, possibly resulting in a heavy mineral signal associated with the full water column.

Most other heavy minerals show occurrence patterns that do not match that of apatite. Although rutile has a high density ($\sim 4.2\,g\,cm^{-3}$), it is significantly enriched in the deposited sediment (Figure 2i), indicating that it can travel in suspension in the lowland Río Bermejo, likely facilitated by seasonal flooding and high sediment concentrations (Moodie et al. 2022), as well as the small size of rutile grains. Being denser than most other minerals, rutile may settle faster and be more rapidly deposited on the floodplain during flooding. Alternatively, higher rutile content in the deposited sediment may be a consequence of winnowing of lighter (lower density) grains during waning overbank flow or later floods, or of its high resistance to dissolution (e.g., Morton and Hallsworth 1999). These factors may lead to enrichment of rutile in the river load upon entrainment of rutile-enriched overbank deposits during channel migration.

Clinopyroxene, amphibole, and tourmaline are more abundant in bedload than in overbank deposits but the heavy-mineral suites of our samples are otherwise notably homogeneous. Such homogeneity, with lack of evidence for significant hydrodynamic-sorting control on heavy-mineral assemblages, permits us to pursue the principal questions posed at the start of this paper.

5.2 | Sediment Weathering in the Lowlands During Deposition

Sediment weathering in the Río Bermejo basin has been previously revealed by secondary clay formation (McGlue et al. 2016) and the downstream increase of river solute concentrations (Repasch et al. 2023). This may have an effect on the mineralogical and textural features of the sediment in the river system. ZTR and percentage of weathered grains are anti-correlated in our sample set (weathered $= 0.89 \times$ ZTR $+ 62.7$, Figure 3a), with suspended sediments carrying the most weathered grains and lower ZTR than deposited sediments, and bedload sediments distributing along the regression line. This is an indicator of weathering and dissolution of minerals in fine-grained overbank deposits, causing the selective breakdown and loss of weathered grains (e.g., labile ferromagnesian silicates) and a relative enrichment in durable minerals. Because the loss of labile minerals involves only ~15% of the bulk heavy mineral composition, which is within the variability of the HMC of our data set, the loss is not significant within the bulk heavy mineral data set. The loss of amphiboles and clinopyroxenes ($Change_X$) from river suspended load and deposits with transit time averages −45% and −61%, respectively. Thereby, the linear loss is statistically significant for clinopyroxenes (Figure 5).

Assuming that weathering of the deposited sediment during floodplain storage is the primary cause of the mineral loss,

the lack of a correlation with deposit ages, ranging from 21 to 1360 years in our sample set (Scheingross et al. 2021; Repasch et al. 2021), suggests that this time span is insufficient to systematically impact weathering indices in the heavy mineral fraction. Instead, compositionally significant weathering must occur on a time scale longer than that covered by our sample set. The weak linear relationship of $Change_X$ with total transit time suggests that this timespan is approaching or exceeds the time required for fine sediment to transit the Río Bermejo foreland, that is, 8520 ± 596 years on average (Repasch et al. 2020) (Figures 2 and 5). Several factors may explain the weak relationship observed between total sediment transit time and the loss of weatherable minerals. First, the dynamic nature of the landscape, characterised by frequent sediment input and remobilization, may prevent the establishment of a clear, linear relationship between sediment age and chemical depletion, particularly over relatively short timescales of less than 10,000 years (Slessarev et al. 2019). Such temporal constraints may limit the detectability of weathering trends, especially in young or rapidly evolving depositional environments. In addition, the already weathered nature of the sediment input in the lowland Río Bermejo may prevent significant weathering within the observed time period.

Studies of other river systems have found evidence of sediment weathering during floodplain storage; for example, Huyghe et al. (2011) interpreted elevated smectite concentrations in shallowly buried Neogene floodplain deposits of the Siwalik Group in NW Nepal as a result of silicate weathering during prolonged sediment residence in the floodplain. Similarly, Yu et al. (2020) observed higher degrees of weathering during more humid intervals over 10,000-year timescales, indicated by an increased smectite/(illite+chlorite) ratio in Bengal Fan deposits. Notably, this trend was only discernible over an 80,000-year record and appeared to be linked to orbital-scale variations in solar insolation. Lastly, it is important to recognize that both total transit times and storage ages represent mixtures of sediments with diverse transport and residence histories. The limited number of analysed samples increases the likelihood of skewed age distributions and may undermine the representativeness of the calculated means. The low R^2 observed in our dataset underscores this issue and calls for a critical examination. Regardless, the combined observations suggest weathering of silicate minerals during floodplain storage, which may capture atmospheric CO_2 on timescales $<10^4$ years (Brady 1991). This CO_2 drawdown could partially offset CO_2 outgassing from mineralization of labile OM in the floodplain (Repasch et al. 2021; Bouchez et al. 2012), but this remains to be quantified. Ongoing floodplain weathering of heavy minerals might also mobilise elements such as Fe, Mg, Ti, Mn and Cu. This promotes the formation of amorphous minerals, including iron hydroxides, and organo-metal complexing (Li et al. 2021; Slessarev et al. 2021; Yan et al. 2015; Vilgé-Ritter et al. 1999; Rose et al. 1998; Mcbride 1994), observed during sediment and carbon storage on timescales of at least 10,000 years in the Río Bermejo floodplain (Scheingross et al. 2021; Repasch et al. 2021).

5.3 | Organic Matter Recycling During Deposition

The *n*-alkane nC_{29} $\delta^{13}C$ values, averaging −32.9‰ ± 5‰ (Figure 4b) reflect the dominant C3 vegetation of the catchment (Powell et al. 2012). The heavy $\delta^{13}C$ value in one bedload sample (AR17-MR30, nC_{29} $\delta^{13}C = -18.4$‰) indicates occasional C4 input to the *n*-alkane fraction. C4 plants are found in agricultural zones along the Río San Francisco (e.g., sampling location AR17-MR30) (Powell et al. 2012). Moreover, heavy *n*-alkane $\delta^{13}C$ values in two deposited sediment samples, combined with the absence of a notable C4 component in other lowland samples, signals either localised influence of C4 vegetation such as annual grasses in the foreland area, rather than a systematic advection of a C4 signal from upstream. Progressive $\delta^{13}C$ enrichment in our chronosequence of Río Bermejo foreland deposits agrees with earlier findings (Scheingross et al. 2021), and could be caused by microbial decomposition (e.g., Bostrom et al. 2007; Ehleringer et al. 2000; Balesdent et al. 1993; Natelhoffer and Fry 1988).

We utilise the altitude effect in *n*-alkanes nC_{29} δ^2H values as first order approximation of OM headwater versus foreland sourcing (Figure 3b,c). However, changes in *n*-alkane δ^2H signatures may reflect catchment-wide sediment integration rather than isolated climatic controls (Chang et al. 2021; Hren and Ouimet 2021). The applied linear regression may underestimate elevation trends, as it is based primarily on northern headwater leaf litter and limited to a narrow elevation range. In contrast, floating OM from southern headwaters exhibits more depleted nC_{29} δ^2H values at higher elevations (Figure 3b). While the northern headwaters contribute >85% of the suspended sediment load and likely dominate the OM supply to the lowland Río Bermejo (Repasch et al. 2020), this suggests the need to refine the regression to better reflect the sources represented in our samples. Given the relatively simple source-to-sink configuration of the Bermejo system, our use of catchment hypsometry remains a reasonable first-order approach for interpreting *n*-alkane sourcing trends.

Following this interpretation, the nC_{29} δ^2H values of all samples indicate admixture of material from the mountain headwaters in many samples (Figure 3b). Notably, bedload sediments have on average lower nC_{29} δ^2H values, indicating more admixture from higher source elevations, even at 865 km downstream (local elevation 60 m asl). We attribute this to bedload samples being sourced mostly from the headwaters, whereas deposited and suspended sediment samples collected downstream are sourced from the foreland. This indicates that bedload sediment is more likely to remain entrained in the lowland channel, and that our bedload samples were not affected by significant admixture from downstream sources. However, with data from a larger number of samples, Dosch, Hovius, Repasch, et al. (2024) have shown that δ^2H values in the bedload of the lowland Río Bermejo can occasionally be heavier, reflecting OM addition from lowland sources. With nC_{29} δ^2H values ranging from −144.0‰ to −123.3‰, the Río Bermejo suspended load and foreland deposits are likely dominantly sourced from local lowland OM below 300 m asl, below the headwater confluence.

Relatively higher CPI values in the deposited sediments, averaging 6.6 ± 1.0 (Figure 4a), suggest post-depositional input of fresh OM during sediment storage in the retroarc foreland basin. The mineral-bound organic carbon is tightly associated with the finest sediment fraction (Repasch et al. 2021, 2020). This carbon has turnover times shorter than the time taken by the fine clastic host particles to transit the Río Bermejo retroarc foreland basin. As a consequence, even the recalcitrant long-chain *n*-alkanes are

substantially degraded and replaced during transit and temporary storage across the lowland river system (Repasch et al. 2021), leading to progressive overprinting of headwater biosignatures. The higher variability of nC_{29} δ^2H values (−132‰ ± 8.6‰) and CPI in deposits compared to the suspended sediment (−139‰ ± 2.6‰; 6.0 ± 0.5) suggest that overbank deposition and later sediment re-entrainment lead to progressive mixing and homogenization of the OM in the suspended load of the active river. In contrast, high variability of bedload CPI (5.7 ± 5) suggests incomplete mixing of OM with different levels of maturity. The low CPI of one bedload sample (AR17MR-31 = 0.31) may reflect a contribution of bedrock-derived petrogenic carbon, even though this is not a major carbon component in the catchment (Scheingross et al. 2021).

5.4 | Combined Proxies Reveal Differences in Source, Routing and Fate of Sediment Types

Combining the sedimentary fingerprints of the siliciclastic and organic river load offers the possibility to distinguish among bedload, suspended load, and deposited sediment and, with that, source imprints versus transit effects on the sediment load. Figure 3c combines information from OM and heavy minerals and offers a systematic comparison of these proxies. While the sediment input into the Rio Bermejo lowland system reflects the source signal, its translation into the system's output is determined by sediment type and transit time, which govern (bio)geochemical reactions acting on both organic and clastic components (Figure 6).

The heavy-mineral assemblage alone does not reveal the location of any compositional alterations, but our observations indicate that sediment enters the modern routing system in a weathered state. The absence of a discernible downstream trend in rounding, ZTR values, and a substantial presence of weathered grains in the bedload (Figure 3a) indicate that a weathering signal may have been imprinted upstream of our sampling locations, for instance via soil erosion, or, more likely, erosion of weathered sedimentary source rock. Low nC_{29} δ^2H values in bedload samples along the river additionally suggest upland OM sourcing and preservation (Figure 3b), and set bedload apart from the suspended and deposited river load (Figure 4c). Organic bedload in the Río Bermejo consists of seemingly fresh plant and woody debris fragments, which can be mobilised during the wet season when approximately

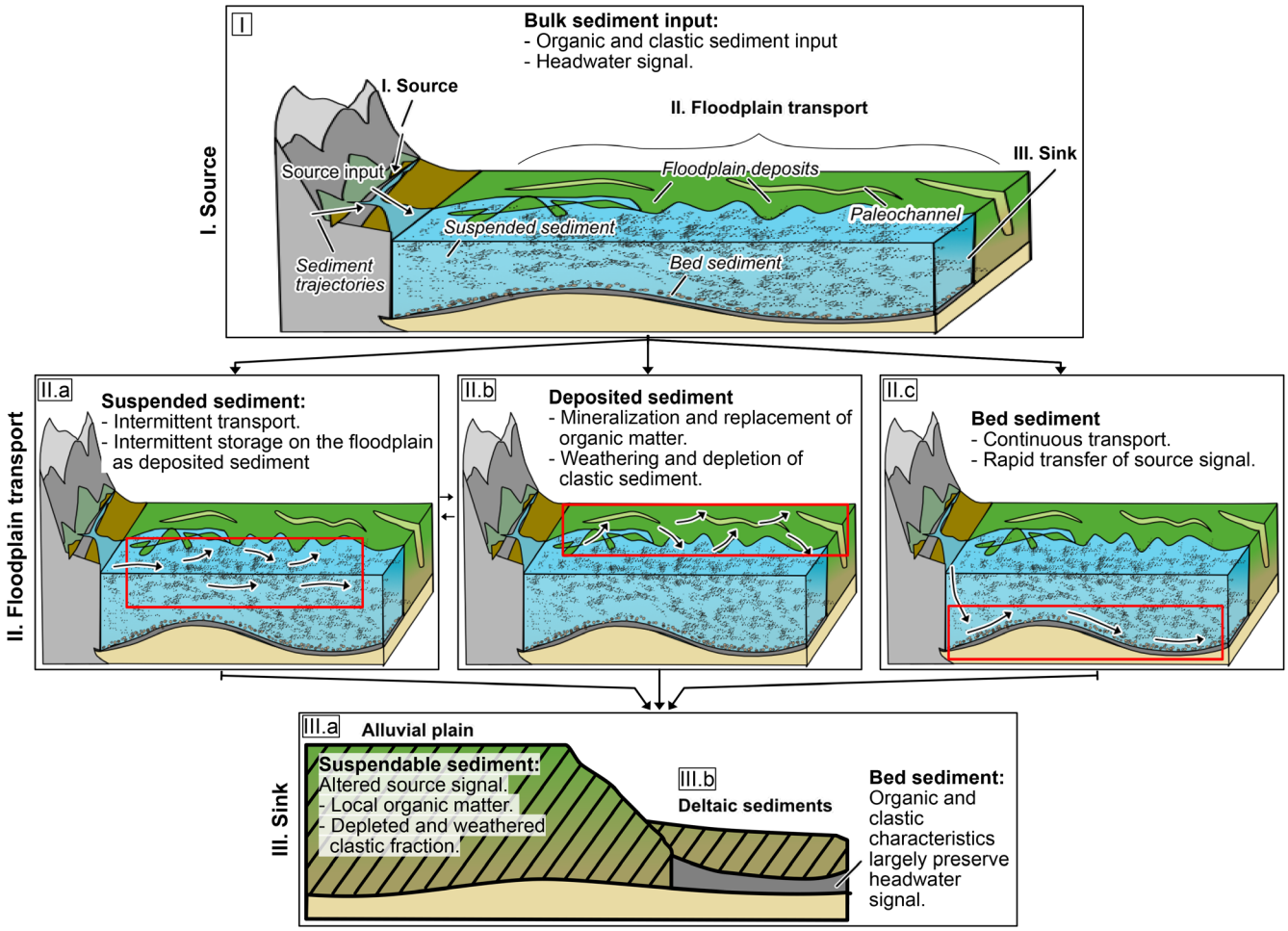

FIGURE 6 | Conceptual diagram summarising organic and clastic sediment pathways and storage processes from source to sink. Panel (I). Source shows relevant floodplain compartments and sediment types, as well as headwater sediment input. Panel (II). Floodplain transport illustrates deposited, suspended, and bed sediment as variable trajectories in foreland transit and how these transport types affect the transmission of source signals. Panel (III). Longitudinal cross-section showing how intermittent floodplain deposition, suspended load, and bedload transport modulate alterations of organic and clastic sediments in alluvial and deltaic sediment deposits.

90% of the river's suspended sediment and discharge are transferred through the lowland section (e.g., Dosch, Hovius, Repasch, et al. 2024; Golombek et al. 2021). However, during the dry season, such transport is absent, and there is no evidence of overbank or floodplain deposition of this bed material. Bedload sediment may be deposited predominantly during major channel avulsions, the most recent of which occurred approximately 150 years ago (Page 1889). Based on these observations, Dosch, Hovius, Repasch, et al. (2024) concluded that bedload transport from the headwater source downstream occurs with limited interruptions and rapidly, likely on seasonal timescales. This rapid and continuous transport likely preserves the heavy-mineral suite, mineral-surface textures, and organic fraction of the headwater source, enabling the quick and conservative export of these sedimentary fingerprints.

In contrast, as suspended sediment spends on average 8520 years in foreland transit, most of this time as deposited sediment in transient overbank storage (Repasch et al. 2020), additional weathering and OM turnover occurs (Repasch et al. 2022; Scheingross et al. 2021, 2019; Haughton et al. 1991). Labile organic carbon undergoes approximately 15–500 turnover cycles during foreland transit (Repasch et al. 2021), resulting in an incorporation of the local, floodplain OM fingerprint, as evidenced by high nC_{29} δ^2H values (Figure 3b,c). The overprinting of upstream-derived sediments by locally produced organic biomarkers has likewise been observed by Brittingham et al. (2025), Galy et al. (2011) and Galy et al. (2008). Consequently, the organic fraction in both deposited and suspended sediments typically reflects local, contemporary retroarc foreland basin conditions over decadal to centennial timescales (Repasch et al. 2021), in contrast to the bedload. Significant compositional effects from sediment weathering and dissolution during foreland transit require cumulative storage time in excess of 10^3 years. Sediment deposited over centennial periods (21–1360 years) exhibits higher ZTR values and lower percentages of weathered grains (Figure 3c), indicating increased stability and resistance to weathering during prolonged storage. In contrast, remobilization of floodplain sediments through lateral channel migration would lead to a progressive accumulation of weathering effects in the suspended load, reflected by higher proportions of weathered grains downstream (Figure 3c).

The weathered state of the suspended sediment sample collected farthest downstream may show the cumulative effect on the river load of multiple cycles of floodplain storage and re-entrainment, the loss of heavy-mineral grains due to dissolution, and the supply of less weathered sediment from the hinterland. We note, however, that a single downstream sample is insufficient to demonstrate this point. Moreover, individual samples taken within a large and articulated river system may reflect local rather than systematic controls on composition. For example, one bedload sample from the upper Río Bermejo (AR17MR27) exhibits a distinct and different composition that does not easily fit with the pattern described above, and could instead represent a highly erosive sediment-supply event located within the humid northern headwater. It is clear that the data set of this study is subjected to high internal variability and thus, limited statistical power in the sedimentological highly homogenised Río Bermejo basin. Nevertheless, our analysis highlights how organic and inorganic sedimentary proxies complement transport and transit processes across varying timescales, and emphasises the need to account for transport and deposition dynamics when interpreting sediment composition.

6 | Conclusion

The combination of heavy minerals and long-chain *n*-alkanes permits the deconvolution and reconstruction of source conditions and processes by considering sediment transport in suspension, as bedload and stored in overbank deposits. The heavy-mineral suite and textures in bedload most faithfully convey the sediment provenance signal through the foreland, and may be used conservatively to deduce sediment provenance in sedimentary deposits. In contrast, suspended and deposited facies may entail both source and weathering effects, which may obscure the original source signal and instead reflect conditions within the alluvial river segments (Jerolmack and Paola 2010). By carefully distinguishing between the composition of bedload and suspended load, and by combining organic and siliciclastic proxies, a more comprehensive view of sediment transport and deposition can be achieved, which may help separate source and transit effects and could provide a more complete systemic picture. This will aid in the interpretation of sedimentary deposits and sediment cycling in active as well as ancient fluvial systems, improving our understanding of spatial and temporal sediment modifications and their role in biogeochemical cycles.

Acknowledgements

We thank Marta Barbarano for her assistance with the heavy mineral sample separation, Gunnar Pruß for his technical support, and Yanina Rojo for her local insight and guidance during the fieldwork. We thank Michael Hren, Jim Pizzuto, and one anonymous reviewer for their detailed and thoughtful reviews, which substantially improved the clarity and rigour of this work. Open Access funding enabled and organized by Projekt DEAL.

Funding

This research was funded by the Deutsche Forschungsgemeinschaft (DFG) and the Federal State of Brandenburg under the auspices of the International Research Training Group IGK2018 'SuRfAce processes, TEctonics and Georesources: The Andean foreland basin of Argentina' (STRATEGy), DFG grant STR 373/34–1 to Manfred Strecker.

Conflicts of Interest

The authors declare no conflicts of interest.

Data Availability Statement

The data that support the findings of this study are openly available as Dosch, Hovius, Ando, et al. (2024) at GFZ Data Services, https://doi.org/10.5880/GFZ.4.6.2024.003.

References

Allen, J. R. L. 1964. "A Review of the Origin and Characteristics of Recent Alluvial Sediments." *Sedimentology* 5: 89–191.

Allison, G. B., C. J. Barnes, M. W. Hughes, and F. W. J. Leaney. 1984. Effect of Climate and Vegetation on Oxygen-18 and Deuterium Profiles in Soils, International Atomic Energy Agency (IAEA), IAEA.

Andò, S., S. Aharonovich, A. Hahn, S. C. George, P. D. Clift, and E. Garzanti. 2019. "Integrating Heavy-Mineral, Geochemical and Biomarker Analyses of Plio-Pleistocene Sandy and Silty Turbidites: A Novel Approach for Provenance Studies (Indus Fan, IODP Expedition 355)." *Geological Magazine* 157: 929–938.

Andò, S., E. Garzanti, M. Padoan, and M. Limonta. 2012. "Corrosion of Heavy Minerals During Weathering and Diagenesis: A Catalog for Optical Analysis." *Sedimentary Geology* 280: 165–178.

Andò, S., A. Morton, and E. Garzanti. 2013. "Metamorphic Grade of Source Rocks Revealed by Chemical Fingerprints of Detrital Amphibole and Garnet." *Geological Society, London, Special Publications* 386: 351–371.

Balesdent, J., C. Girardin, and A. Mariotti. 1993. "Site-Related d13C of Tree Leaves and Soil Organic Matter in a Temperate Forest." *Ecology* 74: 1713–1721.

Bostrom, B., D. Comstedt, and A. Ekblad. 2007. "Isotope Fractionation and 13C Enrichment in Soil Profiles During the Decomposition of Soil Organic Matter." *Oecologia* 153: 89–98.

Bouchez, J., J. Gaillardet, M. Lupker, et al. 2012. "Floodplains of Large Rivers: Weathering Reactors or Simple Silos?" *Chemical Geology* 332-333: 166–184.

Brady, P. V. 1991. "The Effect of Silicate Weathering on Global Temperature and Atmospheric CO2." *Journal of Geophysical Research: Solid Earth* 96: 18101–18106.

Bray, E. E., and E. D. Evans. 1961. "Distribution of n-Paraffins as a Clue to Recognition of Source Beds." *Geochimica et Cosmochimica Acta* 22: 2–15.

Brittingham, A., M. T. Hren, S. Spitzschuch, et al. 2025. "Locally Produced Leaf Wax Biomarkers in the High-Altitude Areguni Mountains Outweigh Downstream Transport." *Biogeosciences* 22: 831–840.

Chang, Q., M. Hren, A. T. Lin, et al. 2021. "Terrestrial Biomarker Isotope Records of Late Quaternary Climate and Source-To-Sink Sediment Transport Processes in Southwestern Taiwan." *American Journal of Science* 321: 393–423.

Chikaraishi, Y., H. Naraoka, and S. R. Poulson. 2004. "Hydrogen and Carbon Isotopic Fractionations of Lipid Biosynthesis Among Terrestrial (C3, C4 and CAM) and Aquatic Plants." *Phytochemistry* 65: 1369–1381.

Cranwell, P. A. 1972. "Chain-Length Distribution of n-Alkanes From Lake Sedimentsin Relation to Post-Glacial Environmental Change." *Freshwater Biology* 2: 259–265.

Dansgaard, W. 1964. "Stable Isotopes in Precipitation." *Tellus* 16: 436–468.

Decelles, P. G. 2012. "Foreland Basin Systems Revisited: Variations in Response to Tectonic Settings." In *Tectonics of Sedimentary Basins. Tectonics of Sedimentary Basins: Recent Advances*, edited by A. A. Busby Cathy. Wiley.

Dellinger, M., R. G. Hilton, J. J. Baronas, et al. 2023. "High Rates of Rock Organic Carbon Oxidation Sustained as Andean Sediment Transits the Amazon Foreland-Floodplain." *Proceedings of the National Academy of Sciences* 120: e2306343120.

Dietrich, W. E. 1982. "Settling Velocity of Natural Particles." *Water Resources Research* 18: 1615–1626.

Dosch, S., N. Hovius, S. Ando, et al. 2024. *Deconvolving the Effects of Fluvial Transit and Storage on Sedimentary Source Signal Preservation Using Heavy Minerals and Terrestrial Biomarkers*. GFZ Data Services.

Dosch, S., N. Hovius, M. Repasch, et al. 2024. "Sourcing and Long-Range Transport of Particulate Organic Matter in River Bedload: Río Bermejo, Argentina." *Earth Surface Dynamics* 12: 907–927.

Dryden, A. L., and C. Dryden. 1946. "Comparative Rates of Weathering of Some Common Heavy Minerals." *Journal of Sedimentary Research* 16: 91–96.

Ehleringer, J. R., N. Buchmann, and L. B. Flanagan. 2000. "Carbon Isotope Ratios in Belowground Carbon Cycle Processes." *Ecological Applications* 10: 412–422.

Elias, S. 2013. *Encyclopedia of Quaternary Science*. Newnes.

Feng, X., S. J. Feakins, Z. Liu, et al. 2016. "Source to Sink: Evolution of Lignin Composition in the Madre de Dios River System With Connection to the Amazon Basin and Offshore." *Journal of Geophysical Research: Biogeosciences* 121: 1316–1338.

Galy, V., T. Eglinton, C. France-Lanord, and S. Sylva. 2011. "The Provenance of Vegetation and Environmental Signatures Encoded in Vascular Plant Biomarkers Carried by the Ganges–Brahmaputra Rivers." *Earth and Planetary Science Letters* 304: 1–12.

Galy, V., C. France-Lanord, and B. Lartiges. 2008. "Loading and Fate of Particulate Organic Carbon From the Himalaya to the Ganga–Brahmaputra Delta." *Geochimica et Cosmochimica Acta* 72: 1767–1787.

Garcin, Y., E. Schefus, V. F. Schwab, et al. 2014. "Reconstructing C 3 and C 4 Vegetation Cover Using n -Alkane Carbon Isotope Ratios in Recent Lake Sediments From Cameroon, Western Central Africa." *Geochimica et Cosmochimica Acta* 142: 482–500.

Garzanti, E. 2017. "The Maturity Myth in Sedimentology and Provenance Analysis." *Journal of Sedimentary Research* 87: 353–365.

Garzanti, E., S. Andó, C. France-Lanord, et al. 2011. "Mineralogical and Chemical Variability of Fluvial Sediments 2. Suspended-Load Silt (Ganga–Brahmaputra, Bangladesh)." *Earth and Planetary Science Letters* 302: 107–120.

Garzanti, E., and S. Andò. 2007. "Chapter 20 Heavy Mineral Concentration in Modern Sands: Implications for Provenance Interpretation." In *Developments in Sedimentology*, edited by M. A. Mange and D. T. Wright. Elsevier.

Garzanti, E., and S. Andò. 2019. "Heavy Minerals for Junior Woodchucks." *Minerals* 9: 148.

Garzanti, E., S. Andò, C. France-Lanord, et al. 2010. "Mineralogical and Chemical Variability of Fluvial sediments1. Bedload Sand (Ganga–Brahmaputra, Bangladesh)." *Earth and Planetary Science Letters* 299: 368–381.

Garzanti, E., S. Andò, and G. Vezzoli. 2020. "Provenance of Cenozoic Indus Fan Sediments (IODP Sites U1456 and U1457)." *Journal of Sedimentary Research* 90: 1114–1127.

Garzanti, E., G. Vezzoli, S. Andò, P. Paparella, and P. D. Clift. 2005. "Petrology of Indus River Sands: A Key to Interpret Erosion History of the Western Himalayan Syntaxis." *Earth and Planetary Science Letters* 229: 287–302.

Golombek, N. Y., J. S. Scheingross, M. N. Repasch, et al. 2021. "Fluvial Organic Carbon Composition Regulated by Seasonal Variability in Lowland River Migration and Water Discharge." *Geophysical Research Letters* 48: e2021GL093416.

Gomez Tapias, J., C. Schobbenhaus, and N. Montes Ramírez. 2019. Geological Map of South America 2019. Scale 1:5000000 Paris Commission for the Geological Map of the World (CGMW), Colombian Geological Survey, and Geological Survey of Brazil.

Greenberg, E., A. J. Chadwick, G. K. Li, and V. Ganti. 2024. "Quantifying Channel Mobility and Floodplain Reworking Timescales Across River Planform Morphologies." *Geophysical Research Letters* 51: e2024GL108537.

Hassenruck-Gudipati, H. J., C. Andermann, S. Dee, et al. 2023. "Moisture Sources and Pathways Determine Stable Isotope Signature of Himalayan Waters in Nepal." *AGU Advances* 4: e2022AV000735.

Haughton, P. D. W., S. P. Todd, and A. C. Morton. 1991. "Sedimentary Provenance Studies." *Geological Society, London, Special Publications* 57: 1–11.

Heijnen, M. S., M. A. Clare, M. J. B. Cartigny, et al. 2022. "Fill, Flush or Shuffle: How Is Sediment Carried Through Submarine Channels to Build Lobes?" *Earth and Planetary Science Letters* 584: 117481.

Hoffmann, B., S. J. Feakins, B. Bookhagen, et al. 2016. "Climatic and Geomorphic Drivers of Plant Organic Matter Transport in the Arun River, E Nepal." *Earth and Planetary Science Letters* 452: 104–114.

Horton, B. K., and P. G. Decelles. 1997. "The Modern Foreland Basin System Adjacent to the Central Andes." *Geology* 25: 895.

Hou, J., W. J. D'andrea, and Y. Huang. 2008. "Can Sedimentary Leaf Waxes Record D/H Ratios of Continental Precipitation? Field, Model, and Experimental Assessments." *Geochimica et Cosmochimica Acta* 72: 3503–3517.

Hren, M. T., and W. Ouimet. 2021. "Organic Molecular Paleohypsometry: A New Approach to Quantifying Paleotopography and Paleorelief." *Frontiers in Earth Science* 9: 665324.

Hubert, J. F. 1962. "A Zircon-Tourmaline-Rutile Maturity Index and the Interdependence of the Composition of Heavy Mineral Assemblages With the Gross Composition and Texture of Sandstones." *Journal of Sedimentary Research* 32: 440–450.

Huyghe, P., R. Guilbaud, M. Bernet, A. Galy, and A. P. Gajurel. 2011. "Significance of the Clay Mineral Distribution in Fluvial Sediments of the Neogene to Recent Himalayan Foreland Basin (West-Central Nepal)." *Basin Research* 23: 332–345.

Jerolmack, D. J., and C. Paola. 2010. "Shredding of Environmental Signals by Sediment Transport." *Geophysical Research Letters* 37: L19401.

Joseph, G. G., R. Zenit, M. L. Hunt, and A. M. Rosenwinkel. 2001. "Particle–Wall Collisions in a Viscous Fluid." *Journal of Fluid Mechanics* 433: 329–346.

Koiter, A. J., P. N. Owens, E. L. Petticrew, and D. A. Lobb. 2013. "The Behavioural Characteristics of Sediment Properties and Their Implications for Sediment Fingerprinting as an Approach for Identifying Sediment Sources in River Basins." *Earth-Science Reviews* 125: 24–42.

Li, H., F. Santos, K. Butler, and E. Herndon. 2021. "A Critical Review on the Multiple Roles of Manganese in Stabilizing and Destabilizing Soil Organic Matter." *Environmental Science and Technology* 55: 12136–12152.

Liu, S., C. Kuhn, G. Amatulli, et al. 2022. "The Importance of Hydrology in Routing Terrestrial Carbon to the Atmosphere via Global Streams and Rivers." *Proceedings of the National Academy of Sciences of the United States of America* 119: e2106322119.

Mann, M. E., R. S. Bradley, and M. K. Hughes. 1999. "Northern Hemisphere Temperatures During the Past Millennium: Inferences, Uncertainties, and Limitations." *Geophysical Research Letters* 26: 759–762.

Märki, L., M. Lupker, A. P. Gajurel, et al. 2020. "Molecular Tracing of Riverine Soil Organic Matter From the Central Himalaya." *Geophysical Research Letters* 47: e2020GL087403.

Mcbride, M. B. 1994. *Environmental Chemistry of Soils*. Oxford University Press.

McGlue, M. M., P. H. Smith, H. Zani, et al. 2016. "An Integrated Sedimentary Systems Analysis of the Rio Bermejo (Argentina): Megafan Character in the Overfilled Southern Chaco Foreland Basin." *Journal of Sedimentary Research* 86: 1359–1377.

Mclennan, S. M., S. Hemming, D. K. Mcdaniel, G. N. Hanson, M. J. Johnsson, and A. Basu. 1993. *Geochemical Approaches to Sedimentation, Provenance, and Tectonics. Processes Controlling the Composition of Clastic Sediments*. Geological Society of America.

Moodie, A. J., J. A. Nittrouer, H. Ma, et al. 2022. "Suspended Sediment-Induced Stratification Inferred From Concentration and Velocity Profile Measurements in the Lower Yellow River, China." *Water Resources Research* 58: e2020WR027192.

Moral Cardona, J. P., J. M. Gutiérrez Mas, A. Sánchez Bellón, S. Domínguez-Bella, and J. Martínez López. 2005. "Surface Textures of Heavy-Mineral Grains: A New Contribution to Provenance Studies." *Sedimentary Geology* 174: 223–235.

Morton, A. C. 1985. "A New Approach to Provenance Studies: Electron Microprobe Analysis of Detrital Garnets From Middle Jurassic Sandstones of the Northern North Sea." *Sedimentology* 32: 553–566.

Morton, A. C., and C. R. Hallsworth. 1999. "Processes Controlling the Composition of Heavy Mineral Assemblages in Sandstones." *Sedimentary Geology* 124: 3–29.

Morton, A. C., and C. R. Hallsworth. 2007. "Stability of Detrital Heavy Minerals During Burial Diagenesis." In *Heavy Minerals in Use*, edited by M. A. Mange and D. T. Wright. Developments in Sedimentology.

Morton, A. C., and D. Smale. 1990. "The Effects of Transport and Weathering on Heavy Minerals From the Cascade River, New Zealand." *Sedimentary Geology* 68: 117–123.

Natelhoffer, K. J., and B. Fry. 1988. "Controls on Natural Nitrogen-15 and Carbon-13 Abundances in Forest Soil Organic Matter." *Soil Science Society of America Journal* 52: 1633–1640.

Nicholls, G. D. 1963. "Environmental Studies in Sedimentary Geochemistry." *Science Progress* 51: 12–31.

Nieto-Moreno, V., A. Rohrmann, M. T. J. Van Der Meer, et al. 2016. "Elevation-Dependent Changes in n -Alkane δ D and Soil GDGTs Across the South Central Andes." *Earth and Planetary Science Letters* 453: 234–242.

Page, J. 1889. "The Gran Chaco and Its Rivers." *Proceedings of the Royal Geographical Society and Monthly Record of Geography* 11: 129–152.

Ponton, C., A. J. West, S. J. Feakins, and V. Galy. 2014. "Leaf Wax Biomarkers in Transit Record River Catchment Composition." *Geophysical Research Letters* 41: 6420–6427.

Powell, R. L., E.-H. Zoo, and C. J. Still. 2012. "Vegetation and Soil Carbon-13 Isoscapes for South America Integrating Remote Sensing and Ecosystem Isotope Measurements." *Ecosphere* 3, no. 11: 109.

Rach, O., X. Hadeen, and D. Sachse. 2020. "An Automated Solid Phase Extraction Procedure for Lipid Biomarker Purification and Stable Isotope Analysis." *Organic Geochemistry* 142: 103995.

Regnier, P., L. Resplandy, R. G. Najjar, and P. Ciais. 2022. "The Land-To-Ocean Loops of the Global Carbon Cycle." *Nature* 603: 401–410.

Repasch, M., J. S. Scheingross, K. L. Cook, et al. 2023. "Lithospheric Flexure Controls on Geomorphology, Hydrology, and River Chemistry in the Andean Foreland Basin." *AGU Advances* 4: e2023AV000924.

Repasch, M., J. S. Scheingross, N. Hovius, et al. 2021. "Fluvial Organic Carbon Cycling Regulated by Sediment Transit Time and Mineral Protection." *Nature Geoscience* 14: 842–848.

Repasch, M., J. S. Scheingross, N. Hovius, et al. 2022. "River Organic Carbon Fluxes Modulated by Hydrodynamic Sorting of Particulate Organic Matter." *Geophysical Research Letters* 49: e2021GL096343.

Repasch, M., H. Wittmann, S. S. Joel, et al. 2020. "Sediment Transit Time and Floodplain Storage Dynamics in Alluvial Rivers Revealed by Meteoric 10Be." *Journal of Geophysical Research. Earth Surface* 125: e2019JF005419.

Resentini, A., S. Andò, and E. Garzanti. 2018. "Quantifying Roundness of Detrital Minerals by Image Analysis: Sediment Transport, Shape Effects, and Provenance Implications." *Journal of Sedimentary Research* 88: 276–289.

Rohrmann, A., M. R. Strecker, B. Bookhagen, et al. 2014. "Can Stable Isotopes Ride Out the Storms? The Role of Convection for Water Isotopes in Models, Records, and Paleoaltimetry Studies in the Central Andes." *Earth and Planetary Science Letters* 407: 187–195.

Rose, J., A. Vilge, G. Olivie-Lauquet, A. Masion, C. Frechou, and J.-Y. Bottero. 1998. "Iron Speciation in Natural Organic Matter Colloids." *Colloids and Surfaces A: Physicochemical and Engineering Aspects* 136: 11–19.

Rouse, H. 1937. "Modern Conceptions of the Mechanics of Fluid Turbulence." *Transactions of the American Society of Civil Engineers* 102: 463–505.

Sachse, D., I. Billault, G. J. Bowen, et al. 2012. "Molecular Paleohydrology: Interpreting the Hydrogen-Isotopic Composition of Lipid Biomarkers From Photosynthesizing Organisms." *Annual Review of Earth and Planetary Sciences* 40: 221–249.

Salio, P., M. Nicolini, and A. C. Saulo. 2002. "Chaco Low-Level Jet Events Characterization During the Austral Summer Season." *Journal of Geophysical Research: Atmospheres* 107: ACL32-1–ACL32-17.

Sambrook Smith, G. H., J. L. Best, J. Z. Leroy, O. Orfeo, and J. Baas. 2016. "The Alluvial Architecture of a Suspended Sediment Dominated Meandering River: The Río Bermejo, Argentina." *Sedimentology* 63: 1187–1208.

Scheingross, J. S., F. Brun, D. Y. Lo, K. Omerdin, and M. P. Lamb. 2014. "Experimental Evidence for Fluvial Bedrock Incision by Suspended and Bedload Sediment." *Geology* 42: 523–526.

Scheingross, J. S., N. Hovius, M. Dellinger, et al. 2019. "Preservation of Organic Carbon During Active Fluvial Transport and Particle Abrasion." *Geology* 47: 958–962.

Scheingross, J. S., M. N. Repasch, N. Hovius, et al. 2021. "The Fate of Fluvially-Deposited Organic Carbon During Transient Floodplain Storage." *Earth and Planetary Science Letters* 561: 116822.

Seluchi, M. E., A. C. Saulo, M. Nicolini, and P. Satyamurty. 2003. "The Northwestern Argentinean Low: A Study of Two Typical Events." *Monthly Weather Review* 131: 2361–2378.

Sklar, L. S. 2024. "Grain Size in Landscapes." *Annual Review of Earth and Planetary Sciences* 52: 663–692.

Slessarev, E. W., O. A. Chadwick, N. W. Sokol, E. E. Nuccio, and J. Pett-Ridge. 2021. "Rock Weathering Controls the Potential for Soil Carbon Storage at a Continental Scale." *Biogeochemistry* 157: 1–13.

Slessarev, E. W., X. Feng, N. L. Bingham, and O. A. Chadwick. 2019. "Landscape Age as a Major Control on the Geography of Soil Weathering." *Global Biogeochemical Cycles* 33: 1513–1531.

Stewart, M. K., and C. B. Taylor. 1981. "Environmental Isotopes in New Zealand Hydrology; 1 Introduction the Role of Oxygen-18, Deuterium, and Tritium in Hydrology." *New Zealand Journal of Science* 24: 295–311.

Stieglitz, R. D., and B. Rothwell. 1978. "Surface Microtextures of Freshwater Heavy Mineral Grains." *Geoscience Wisconsin* 3: 21–34.

Strosser, E. 2010. "Methods for Determination of Labile Soil Organic Matter: An Overview." *Journal of Agrobiology* 27: 49–60.

Tejan-Kella, M. S., D. J. Chittleborough, and R. W. Fitzpatrick. 1991. "Weathering Assessment of Heavy Minerals in Age Sequences of Australian Sandy Soils." *Soil Science Society of America Journal* 55: 427–438.

Tipple, B. J., and M. Pagani. 2013. "Environmental Control on Eastern Broadleaf Forest Species' Leaf Wax Distributions and D/H Ratios." *Geochimica et Cosmochimica Acta* 111: 64–77.

Tofelde, S., A. Bernhardt, L. Guerit, and B. W. Romans. 2021. "Times Associated With Source-To-Sink Propagation of Environmental Signals During Landscape Transience." *Frontiers in Earth Science* 9: 628315.

Vera, C., W. Higgins, J. Amador, et al. 2006. "Toward a Unified View of the American Monsoon Systems." *Journal of Climate* 19: 4977–5000.

Vilgé-Ritter, A., J. Rose, A. Masion, J. Y. Bottero, and J. M. Lainé. 1999. "Chemistry and Structure of Aggregates Formed With Fe-Salts and Natural Organic Matter." *Colloids and Surfaces A: Physicochemical and Engineering Aspects* 147: 297–308.

Walker, C. D., and S. B. Richardson. 1991. "The Use of Stable Isotopes of Water in Characterising the Source of Water in Vegetation." *Chemical Geology: Isotope Geoscience Section* 94: 145–158.

Yan, M., Y. Lu, Y. Gao, M. F. Benedetti, and G. V. Korshin. 2015. "In-Situ Investigation of Interactions Between Magnesium Ion and Natural Organic Matter." *Environmental Science and Technology* 49: 8323–8329.

Yu, Z., C. Colin, F. Bassinot, S. Wan, and G. Bayon. 2020. "Climate-Driven Weathering Shifts Between Highlands and Floodplains." *Geochemistry, Geophysics, Geosystems* 21: e2020GC008936.

Ziegler, H., C. B. Osmond, W. Stichler, and P. Trimborn. 1976. "Hydrogen Isotope Discrimination in Higher Plants: Correlations With Photosynthetic Pathway and Environment." *Planta* 128: 85–92.

Supporting Information

Additional supporting information can be found online in the Supporting Information section. **Figure S1:** (a) Cumulative grain-size distribution for all samples; (b) median grain size (D_{50}) of each sample with downstream distance from mountain front. Suspended and bed sediment data previously published by Scheingross et al. (2021). **Figure S2:** Median grain size (D_{50}, μm) and selected heavy minerals; (a) apatite, (b) rutile, (c) amphibole, (d) sum of angular, rounded and subrounded tourmaline, (e) clinopyroxene, and (d) percentage of weathered grains. Linear regressions in panels (a and b) were calculated using all data points. Regression was significant only for apatite ($p < 0.01$). **Figure S3:** Heavy mineral assemblage of the deposited sediments. *x*-axis labelled after depositional age: deposited sediment sites as young overbank depists close to the active channel, sediments with deposit age of min. 150 years, ca. 14 km from the active channel, and sediments with depositional age of 60–1360 years, ca. 15 km away from the active channel. (a) Total heavy mineral concentration (HM, w.%), (b) transparent heavy mineral concentration (tHM, w.%), (c) Hornblende Colour Index (HCI), (d) Zircon-Tourmaline-Rutile (ZTR) index, as well as the percentage (grain count per 200 grains per sample) of common heavy minerals: (e) amphibole, (f) apatite, (g) clinopyroxene, (h) epidote, (i) rutile, (j) titanite, (k) titanium oxides, (l) tourmaline, (m) zircon, and percentage of (n) rounded and (o) weathered grains.